UC Santa Barbara
UC Santa Barbara Previously Published Works

Title

Three-Dimensional Spin Texture in Hybrid Perovskites and Its Impact on Optical Transitions

Permalink

https://escholarship.org/uc/item/3zb6h766

Journal

The Journal of Physical Chemistry Letters, 9(11)

ISSN

1948-7185

Authors

Zhang, Xie
Shen, Jimmy-Xuan
Van de Walle, Chris G

Publication Date

2018-06-07

DOI

10.1021/acs.jpclett.8b01004

Peer reviewed

Three-dimensional Spin Texture in Hybrid Perovskites and Its Impact on Optical Transitions

Xie Zhang,[*,†,¶] Jimmy-Xuan Shen,[‡,¶] and Chris G. Van de Walle[*,†]

†*Materials Department, University of California, Santa Barbara, CA 93106-5050, U.S.A.*

‡*Department of Physics, University of California, Santa Barbara, CA 93106-9530, U.S.A.*

¶*Contributed equally to this work*

E-mail: xiezhang@ucsb.edu; vandewalle@mrl.ucsb.edu

Abstract

Hybrid perovskites such as $MAPbI_3$ ($MA=CH_3NH_3$) exhibit a unique spin texture. The spin texture (as calculated within the Rashba model) has been suggested to be responsible for a suppression of radiative recombination due to a mismatch of spins at the band edges. Here we compute the spin texture from first principles and demonstrate that it does *not* suppress recombination. The exact spin texture is dominated by the inversion asymmetry of the local electrostatic potential, which is determined by the structural distortion induced by the MA molecule. In addition, the rotation of the MA molecule at room temperature leads to a dynamic spin texture in $MAPbI_3$. These insights call for a reconsideration of the scenario that radiative recombination is suppressed, and provide an in-depth understanding of the origin of the spin texture in hybrid perovskites, which is crucial for designing spintronic devices.

Graphical TOC Entry
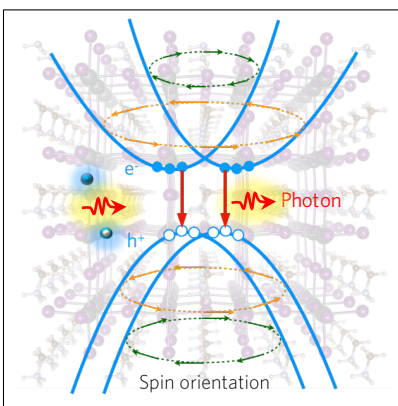
Hybrid perovskites have attracted tremendous attention due to their excellent photovoltaic efficiency, already reaching a record of ~22%[1] just a few years after their first application as solar-cell materials in 2009.[2] This superior performance has been attributed to a long carrier lifetime, which can be on the order of 1 μs.[3] Multiple explanations for this long lifetime have been suggested, including formation of ferroelectric domains,[4] photon recycling,[5] formation of large polarons,[6] and momentum[7] or spin mismatch[8] between the lowest conduction band (CB) and the highest valence band (VB). Among the proposed schemes for suppressing recombination, the spin-mismatch model is particularly intuitive and has triggered multiple follow-up studies.[9–15]

A schematic of the model proposed by Zheng *et al.*[8] is presented in Figure 1a, showing how a spin-forbidden transition can limit carrier recombination. Due to strong spin-orbit coupling (SOC) and a lack of inversion symmetry, the bands near the R point split into two bands with opposite spin orientations (green and orange arrows). According to ref. 8 the CB and VB edges split in different ways, leading to spin mismatch between the lowest CB and the highest VB. At the low carrier densities found in solar cells, most of the charge carriers occupy states near the band edges; therefore the spin mismatch greatly suppresses direct radiative recombination between photoexcited electrons and holes and increases the carrier lifetime.

The spin-forbidden transition model[8] is based on the spin texture obtained from a parametrized two-dimensional (2D) Rashba effective model.[16,17] The applicability of this model to three-dimensional (3D) bulk materials has not been established. In the present study we address this issue by computing the spin texture in MAPbI$_3$ (MA=CH$_3$NH$_3$) completely from first principles (see the Methods section).

We find that the SOC-induced momentum splitting of the CBs and VBs occurs in a coherent way, resulting in matching spins at the CB and VB edges, and thus the direct optical transition remains allowed (see Figure 1b). Our results show that in bulk SOC materials the spin texture does not follow a fixed pattern, but varies based on the examined
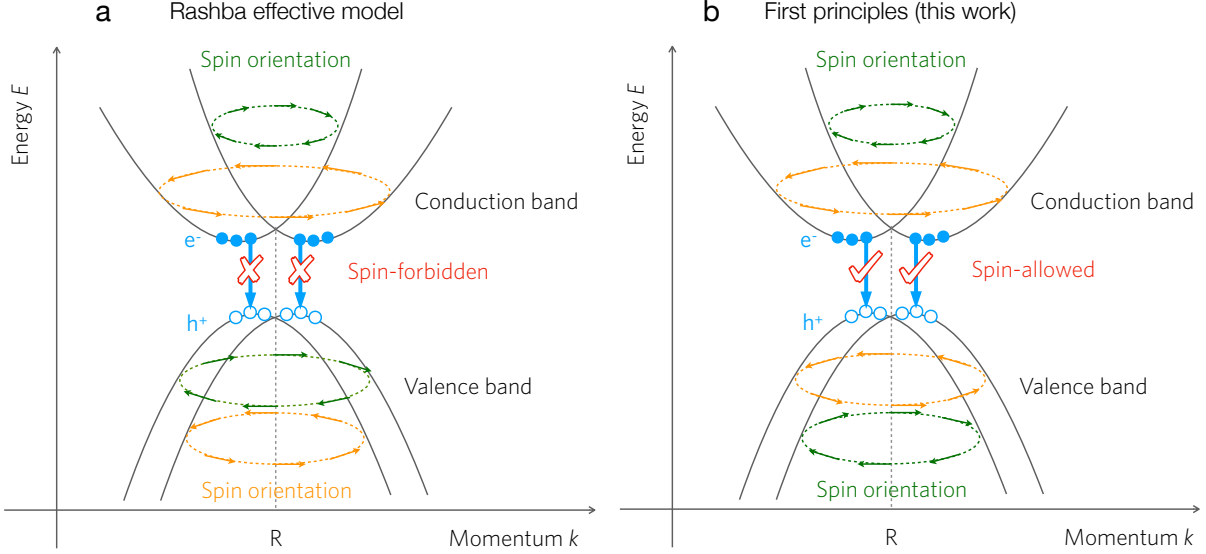
3

Figure 1: (a) Schematic of the spin-forbidden transition model proposed in the literature.[8] (b) Schematic of the spin-allowed transition obtained in this work using first principles. Bands are shown in the vicinity of the band extrema at the R point in the Brillouin zone. The green and orange arrows represent the helical spin orientations in different bands. Blue solid and open circles denote photoexcited electrons (e^-) and holes (h^+), respectively.

cross section of the Brillouin zone. We will demonstrate that the characteristics of the spin texture are governed by the inversion asymmetry of the local electrostatic potential, which is determined by the structural distortion of the inorganic lattice induced by the MA molecule. In addition, we find that the spin texture is dynamic, since the MA molecule is rotating at room temperature. Overall, our accurate determination of the spin texture disproves the spin-forbidden transition model in the literature, and also provides essential information in light of proposed applications of the hybrid perovskites for spintronic devices.[18–20]

Figure 2a depicts the computed band structure of cubic $MAPbI_3$ with the MA molecule oriented along the [100] direction. All atoms are fully relaxed within a cubic shape after initializing the MA molecule to the [100] direction. The CB and VB both exhibit some degree of linear-k momentum splitting at the R point, but the splitting of the CB is more pronounced. This is because the lowest CB is comprised mainly of Pb p states, while the highest VB has mostly I p character. The Pb atom is much heavier than the I atom and has a stronger SOC effect. The momentum splittings therefore lead to a slightly indirect band
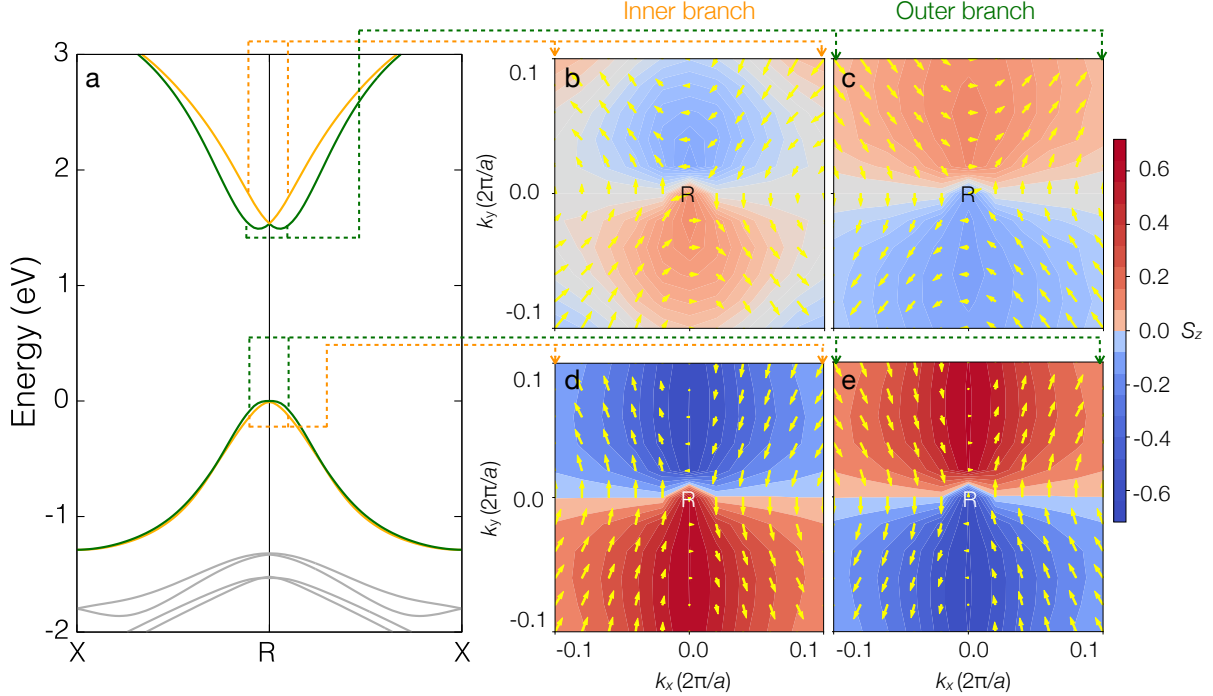
4

Figure 2: (a) Calculated band structure of MAPbI$_3$ with the MA molecule oriented along [100]. (b−e) The corresponding spin texture of the lowest two CBs and the highest two VBs for a slice ($k_z = 0.5$ in units of $2\pi/a$) of **k** points in the Brillouin zone. The coordinates of the **k** points are defined relative to the R point (0.5, 0.5, 0.5). The yellow arrows represent (S_x, S_y), while the background color denotes the third component, S_z, where (S_x, S_y, S_z) are the expectation values of the spinor operator.

gap. Detailed quantification of the spin-splitting parameters can be found in, e.g., ref. 21. In this paper we focus on the spin texture.

In Figure 2b−d we show the spin texture of the two lowest CBs and the two highest VBs for a slice of **k** points perpendicular to the z axis (all k values will be expressed in units of $2\pi/a$). The expectation values of the 3D spinors are visualized as 2D vectors using the S_x and S_y components, and the S_z component is represented by the background color. These figures convey two important messages. First, the split CBs (or VBs) indeed have opposite spin orientations. However, the inner branches of CB and VB have the *same* spin orientation. The same applies to the outer branches. This clearly shows that the optical transition between the lowest CB and the highest VB is not spin-forbidden. Second, the spin texture of both the CBs and VBs is qualitatively different from the helical spin texture

5

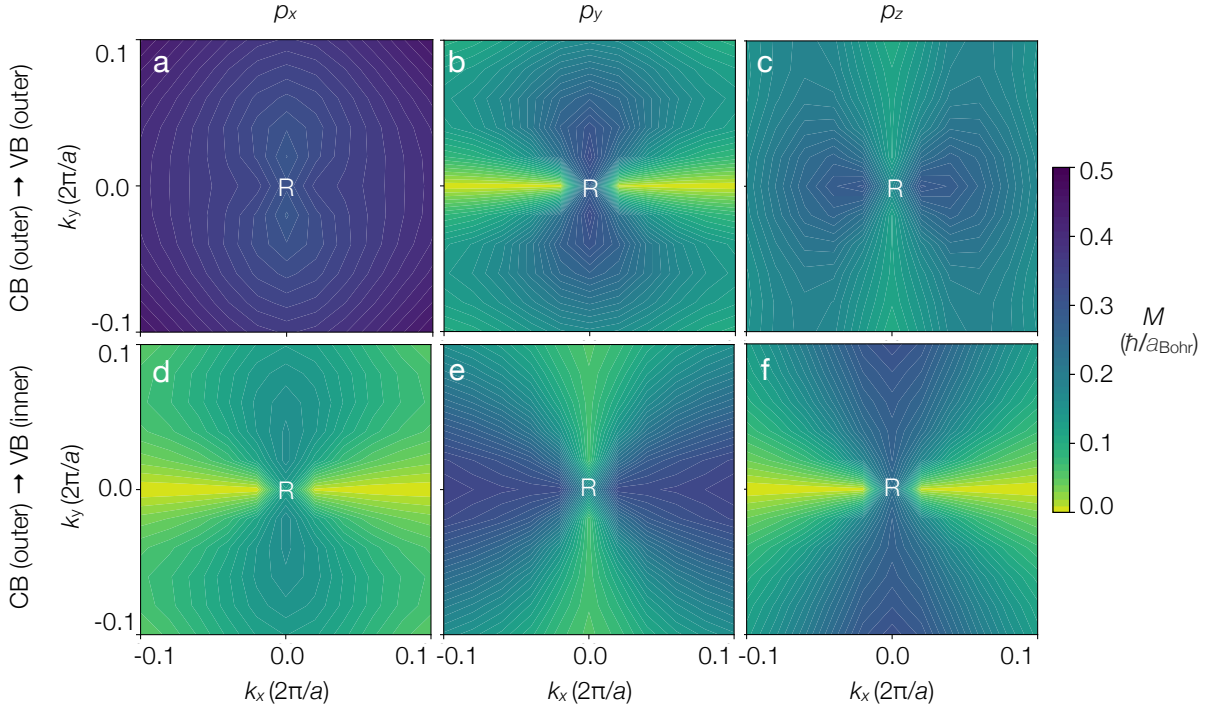obtained from the Rashba effective model of ref. 8. In the following, we discuss these two points in detail.

Figure 3: (a−c) Matrix elements of momentum (p_x, p_y and p_z) of the CB(outer)→VB(outer) transition. (d−f) Momentum matrix elements of the CB(outer)→VB(inner) transition. **k**-point slices are defined as in Figure 2.

Impact of spin on optical transitions. The optical transition between the lowest CB and the highest VB is not spin-forbidden. To examine the nature of the transition, we compute the momentum matrix elements **M** in the vicinity of the R point: $|k_i - R_i| \leq 0.1$ ($2\pi/a$), where $i = x$, y and z; this range covers the states that are occupied by photoexcited electrons and holes at carrier densities up to 10^{18} cm^{-3}. Figure 3 shows the matrix elements of momentum (p_x, p_y and p_z) between the lowest CB and the two highest VBs. By comparing Figure 3a−c with Figure 3d−f, we can see that the spin texture indeed significantly affects the momentum matrix elements. For the p_x component, the CB(outer)→VB(outer) transition exhibits particularly large momentum matrix elements ($\sim 0.4-0.5$ $\hbar/a_{Bohr}$, where a_{Bohr} is the Bohr radius), while the CB(outer)→VB(inner) transition is nearly zero due to the mismatched spins. For the other two components, even though the transitions are weaker

6

than for the p_x component, both the CB(outer)→VB(outer) and the CB(outer)→VB(inner) transitions still exhibit sizable momentum matrix elements over a large range of **k** points. As a comparison, we find that the momentum matrix elements of the CB(outer)→VB(outer) transition are similar to the ones when SOC is switched off for the same structure. Overall, we can conclude that the optical transitions between the band edges are not spin-forbidden (see Figure 1b). Our calculations (using the methodology described in ref. 22) show that momentum matrix elements of the calculated magnitude lead to a direct radiative recombination coefficient around 10^{-10} cm^{3}s^{-1} for typical carrier densities ($10^{14} - 10^{17}$ cm^{-3}) at room temperature, in good agreement with experimental measurements[23] and close to the values in efficient optoelectronic materials such as GaAs (7.2×10^{-10} cm^{3}s^{-1}[23]).

Inadequacy of the Rashba effective model. A close inspection of the spin texture in Figure 2b−e shows that it resembles the Dresselhaus,[24] rather than the Rashba[16] spin texture (detailed descriptions of Dresselhaus and Rashba spin textures can be found in ref. 25). To understand the fundamental reasons, we revisit the basic formalisms for SOC. In the Rashba effective model,[16] the SOC Hamiltonian is expressed as

$$H_{\mathrm{SOC}} = \alpha(\hat{S}_x k_y - \hat{S}_y k_x)\,, \tag{1}$$

while a 2D version of the Dresselhaus SOC Hamiltonian[24] is defined by

$$H_{\mathrm{SOC}} = \beta(\hat{S}_x k_x - \hat{S}_y k_y)\,. \tag{2}$$

In our first-principles approach for 3D SOC, the perturbative Hamiltonian is given by

$$
\begin{aligned}
H_{\text{SOC}} =& \frac{\hbar}{4m_e^2 c^2} \hat{\mathbf{S}} \cdot (\nabla \mathbf{V} \times \hat{\mathbf{p}}) \\
=& \frac{\hbar}{4m_e^2 c^2} \nabla \mathbf{V} \cdot (\hat{\mathbf{p}} \times \hat{\mathbf{S}}) \\
=& \frac{\hbar^2}{4m_e^2 c^2} \left[\nabla_x V (\hat{S}_z k_y - \hat{S}_y k_z) + \nabla_y V (\hat{S}_x k_z - \hat{S}_z k_x) \right. \\
& \left. + \nabla_z V (\hat{S}_y k_x - \hat{S}_x k_y) \right],
\end{aligned}
\tag{3}
$$

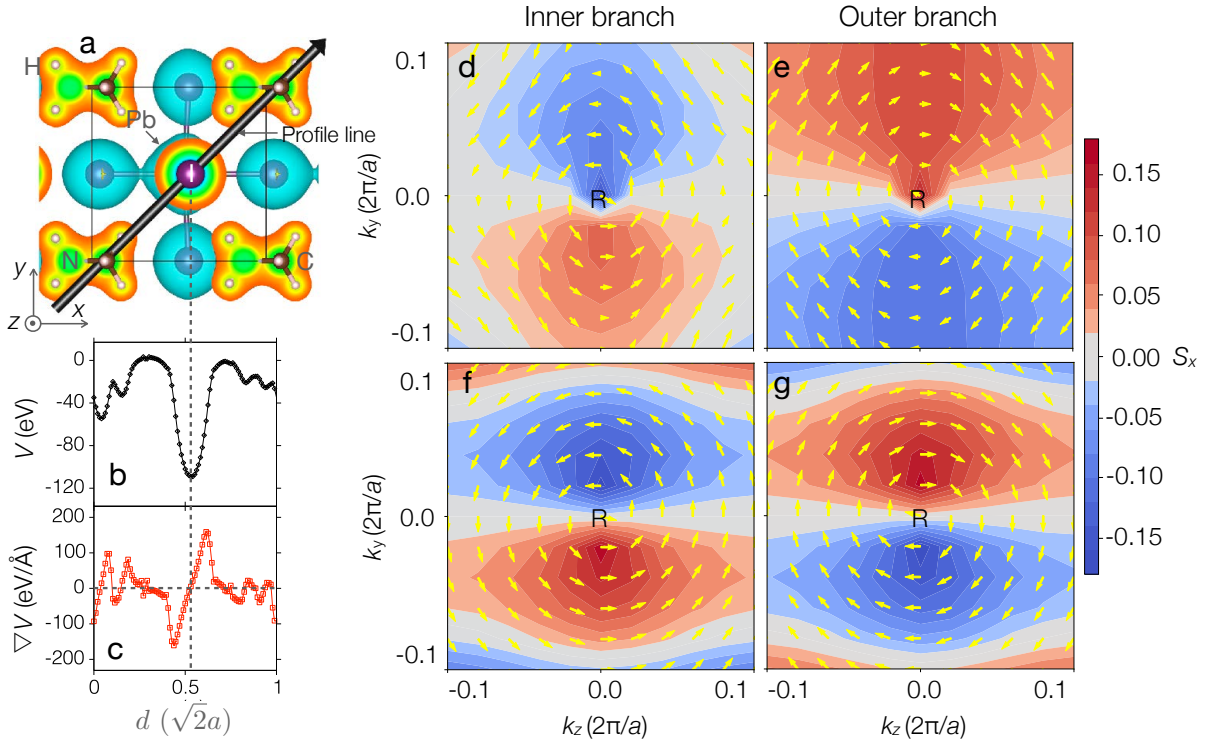where m_e is the electron mass, c is the speed of light, and V is the local electrostatic potential.

Figure 4: (a) Isosurface of the local electrostatic potential (V) in MAPbI$_3$ with the MA molecule oriented along [100]. (b) A line profile of V as a function of distance d (in units of $\sqrt{2}a$) along the [110] direction as shown by the black arrow through the I atom in (a). (c) The corresponding gradient of the local electrostatic potential. (d−g) The spin texture of the lowest two CBs (d−e) and the highest two VBs (f−g). Unlike in Figure 2, the slice of $\mathbf{k}$ points is defined by $k_x = 0.5$. The (S_z, S_y) vector is represented by the yellow arrows and S_x is shown by the background color.

Equation 3 shows that the perturbative SOC Hamiltonian is actually governed by the *gradient* of the local electrostatic potential. Figure 4a displays an isosurface of the computed

8

local electrostatic potential from first principles. The presence of the MA molecule induces an inversion asymmetry of the lattice by distorting the Pb-I octahedron and thus also an inversion asymmetry of the local electrostatic potential. Indeed, if we fix the Pb and I atoms to their ideal positions in a perovskite structure, then the inversion symmetry is retained and the splitting almost vanishes. More insight can be gained by examining the values along a fixed direction. In Figure 4b we show a line profile of the local electrostatic potential V along the [110] direction (indicated by the black arrow through the I atom in Figure 4a). Due to the presence of the MA molecule, V lacks inversion symmetry, which means that ∇V (see Figure 4c) is no longer an odd function with respect to the I atom at the face center of the cell. $\nabla_x V$, $\nabla_y V$, and $\nabla_z V$ are evaluated using a finite-difference approach on a dense mesh ($96 \times 96 \times 96$) for the unit cell.

To quantitatively capture this effect, we compute $\langle \nabla_x V \rangle$, $\langle \nabla_y V \rangle$, and $\langle \nabla_z V \rangle$ by averaging $\nabla_x V$, $\nabla_y V$, and $\nabla_z V$ over the unit cell. If the structure (and thus the potential) has inversion symmetry, then $\langle \nabla_x V \rangle$, $\langle \nabla_y V \rangle$, and $\langle \nabla_z V \rangle$ are all zero. The value of $\langle \nabla V \rangle$ is thus a measure of the inversion asymmetry of V. We recognize that more sophisticated measures could be employed to quantify the inversion asymmetry, e.g., the electric polarization,[26] or an expectation value of ∇V that takes into account the overlap of relevant wavefunctions. For our purposes in the present study, $\langle \nabla V \rangle$ is adequate as a simple but effective measure of the polarization. The results are tabulated in Table 1 for different orientations of the MA molecule.

Table 1: Average of the gradient of the local electrostatic potential (in units of meV/Å) in MAPbI₃ with the MA molecule oriented along the [100], [110] and [111] directions.

MA orientation	$\langle \nabla_x V \rangle$	$\langle \nabla_y V \rangle$	$\langle \nabla_z V \rangle$
[100]	3.271	-0.284	-0.699
[110]	0.727	0.484	-0.001
[111]	1.875	1.875	1.875

For the case with the MA molecule oriented along the [100] direction, $\langle \nabla_x V \rangle$ is much larger than $\langle \nabla_y V \rangle$ and $\langle \nabla_z V \rangle$. Therefore, the Hamiltonian in eq 3 is dominated by the
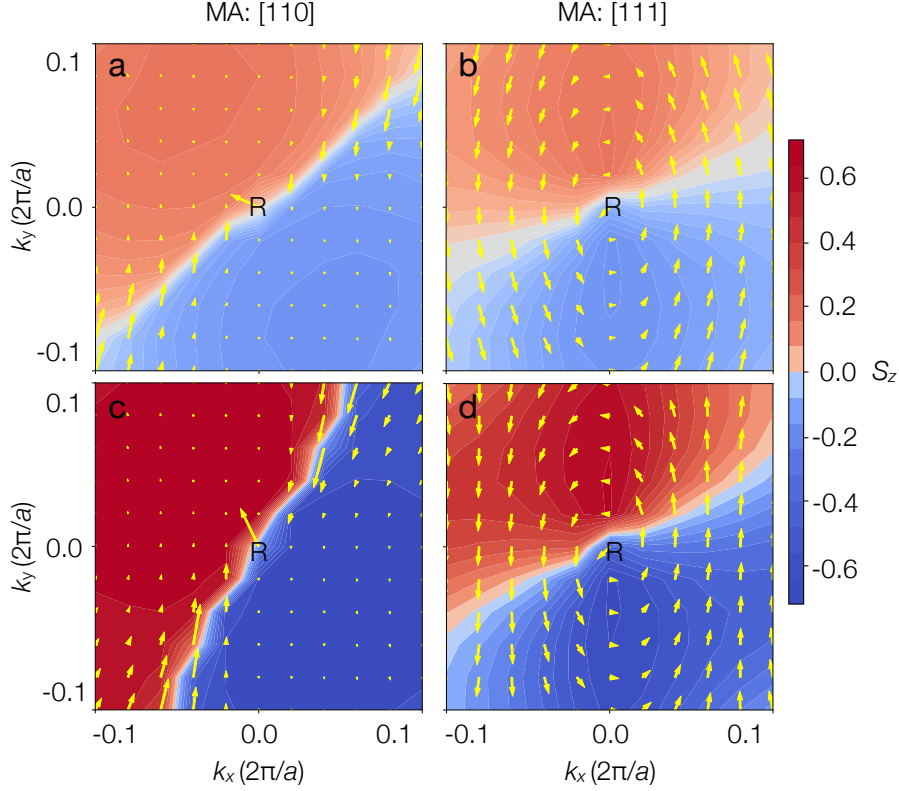
Figure 5: Spin texture of (a, b) the lowest CB and (c, d) the highest VB in MAPbI$_3$ with the MA molecule oriented (a, c) along the [110] direction and (b, d) along the [111] direction. **k**-point slices are defined as in Figure 2.

$\nabla_x V(k_y \hat{S}_z - k_z \hat{S}_y)$ term, which is similar to the 2D Rashba model as shown in eq 1. Such a simplified Hamiltonian indicates that there will be a helical-type spin texture between S_y and S_z components on a (k_y, k_z) plane according to the Rashba formalism. Indeed, this is evident from Figure 4d−g, which depicts the spin texture plotted in a slice of the Brillouin zone perpendicular to the x axis ($k_x = 0.5$): the spin texture clearly follows a Rashba-type helical pattern, confirming our arguments above. But this simple pattern only emerges for this particular choice of **k**-point slice! As shown in Figure 2b−e, a different choice of **k**-point slice results in a very different spin texture that does not look Rashba-like at all. We conclude that in bulk materials with strong SOC effects the spin texture does not follow a fixed pattern, but depends on which cross section of the Brillouin zone is being examined. If the inspected plane is perpendicular to the polarization direction, the spin texture can

be captured by the Rashba effective model. Irrespective of the specific pattern in the spin texture, we see in Figure 4d−g that the spin does *not* suppress the optical transitions, a consistent trend also found in Figure 2b−e.

If the Rashba effective model (eq 1) is applied as a constant perturbation (fixed α value), it correctly describes the helical spin texture, but results in band edges that always have mismatched spins, a consequence of the effective mass of holes having opposite sign to that of electrons. As shown by Zheng *et al.*,[8] different perturbations can be applied to each of the band edges by projecting the Hamiltonian onto separate 2×2 Hamiltonians for the VB and CB. Changing the *magnitude* of α then represents different strength of Rashba splitting for the VB and CB, but to capture the correct spin orientation also the *sign* of α should be reversed for the VB relative to the CB.

Since the spin texture is directly related to the gradient of the local electrostatic potential that is determined by the structural distortion induced by the MA molecule, one expects the spin texture to change depending on this orientation, similar to what was shown by Stroppa *et al.*[18] for tin iodide perovskites. In Figure 5, we show the spin texture of the lowest CB and the highest VB for the same **k**-point slice ($k_z = 0.5$) as in Figure 2, but with the MA molecule oriented along two different high-symmetry directions ([110] and [111]). The spin texture is clearly different from the result shown in Figure 2, where the MA molecule is oriented along the [100] direction.

For the case of the MA molecule oriented along the [110] direction, the pattern of the spin texture corresponds to neither the Rashba nor the Dresselhaus model. The small values for the S_x and S_y components and large value for S_z imply an almost collinear spin texture along the z direction. This can be understood again on the basis of eq 3: the MA molecule induces an inversion asymmetry of the local electrostatic potential mainly along the [110] direction and $\langle \nabla_z V \rangle$ is negligibly small (see Table 1). Hence, very weak Rashba SOC is expected for the **k**-point slice of k_z=0.5, which is confirmed by Figure 5a,c.

When the MA molecule is oriented along the [111] direction, $\langle \nabla_x V \rangle$, $\langle \nabla_y V \rangle$, and $\langle \nabla_z V \rangle$

are equal in magnitude (see Table 1), which indicates that we should be able to observe Rashba-type spin texture for all three **k**-point slices ($k_x = 0.5$, $k_y = 0.5$, and $k_z = 0.5$). This is indeed the case (see Figure 5b,d for the spin texture of the $k_z = 0.5$ slice). Again, we note that the spin texture does not suppress the optical transitions, for all orientations of the MA molecule.

The variation of the spin texture with changing the **k**-point slice of the Brillouin zone demonstrates that the spin texture in bulk SOC materials should be characterized within a 3D framework. First-principles approaches are capable of treating this complication, but one needs to keep in mind that the specific pattern of the spin texture is tied to a specific atomic structure. As we have pointed out, the MA molecule can assume different orientations in MAPbI$_3$. Since the rotation barrier is only $\sim$20 meV,[27] the orientation of the MA molecule is dynamically changing at room temperature. As we have shown, structures with different MA orientations have different spin texture, which therefore implies a dynamic spin texture in MAPbI$_3$ as suggested by Etienne *et al.*[13]

To conclude, we have computed the spin texture in the prototypical hybrid perovskite, MAPbI$_3$, employing a first-principles approach. It was found that the spin texture in MAPbI$_3$ enables spin-matched direct optical transitions, disproving the spin-forbidden transition model in the literature. Further, we showed that in bulk MAPbI$_3$ the spin texture follows different patterns on different slices of **k** points in the Brillouin zone. The exact pattern in the spin texture is essentially determined by the inversion asymmetry of the local electrostatic potential. Since the MA molecule is rotating even at room temperature and the spin texture varies when changing the MA orientation, MAPbI$_3$ will exhibit a dynamic spin texture. These insights help us to understand the spin texture in bulk SOC materials and pave the way for making better use of the strong SOC in hybrid perovskites to design potential spintronic devices.

Methods

Our first-principles calculations are based on density-functional theory using the Vienna *Ab-initio* Simulation Package (VASP).[28] A fraction of screened Fock exchange $\alpha = 0.55$ in the Heyd-Scuseria-Ernzerhof functional[29] produces an accurate description for the band structure of cubic MAPbI$_3$ with a band gap of 1.55 eV, within the experimentally reported range of $1.5-1.6$ eV.[30] The projector augmented wave (PAW) approach[31] is employed with a plane-wave energy cutoff E_{cut}=500 eV. The first Brillouin zone of the 12-atom unit cell is sampled with a $4 \times 4 \times 4$ Monkhorst-Pack[32] **k**-point grid. Convergence of eigenvalues and spin texture was tested by using a $6 \times 6 \times 6$ grid. Volume and atomic positions were relaxed (residual forces < 0.01 eV/Å) within a cubic shape. The optimized lattice constant is 6.348 Å, in good agreement with experiment (6.32 Å[33]). For structural relaxations, we first orient the MA molecule along the high-symmetry directions, and then fully relax all atomic positions within a fixed cubic shape. Local minima exist in the potential energy surface as a function of the orientation of the MA molecule; the molecule can be oriented along the [100], [110] or [111] directions.

SOC is taken into account by applying a perturbation $\sum_{i,l,m} V_l^{\text{SOC}} \mathbf{L} \cdot \mathbf{S} |l,m,i\rangle\langle l,m,i|$ to the pseudopotential. The spin texture is evaluated by projecting the calculated wavefunctions $|\psi\rangle$ on the spin and orbital basis of each atomic site $S_n^{i,l,m} = \langle\psi_n|(S_n \otimes |l,m,i\rangle\langle l,m,i|)|\psi_n\rangle$ and then summing $S_n^{i,l,m}$ for a given spin direction n and all atomic sites in the unit cell.[34]

The momentum matrix elements between a CB (c) and a VB (v) are computed in reciprocal space using[35]

$$\mathbf{M}_{\text{cv}}(\mathbf{k}) = \langle\psi_{\text{c}}|\mathbf{p}|\psi_{\text{v}}\rangle, \tag{4}$$

where ψ_{c} (ψ_{v}) is the wavefunction of the CB c (VB v) and $\mathbf{p}$ is the momentum operator.

Acknowledgement

References

(1) Yang, W. S.; Park, B.-W.; Jung, E. H.; Jeon, N. J.; Kim, Y. C.; Lee, D. U.; Shin, S. S.; Seo, J.; Kim, E. K.; Noh, J. H. et al. Iodide management in formamidinium-lead-halide-based perovskite layers for efficient solar cells. *Science* **2017**, *356*, 1376–1379.

(2) Kojima, A.; Teshima, K.; Shirai, Y.; Miyasaka, T. Organometal halide perovskites as visible-light sensitizers for photovoltaic cells. *J. Am. Chem. Soc.* **2009**, *131*, 6050–6051.

(3) Shi, D.; Adinolfi, V.; Comin, R.; Yuan, M.; Alarousu, E.; Buin, A.; Chen, Y.; Hoogland, S.; Rothenberger, A.; Katsiev, K. et al. Low trap-state density and long carrier diffusion in organolead trihalide perovskite single crystals. *Science* **2015**, *347*, 519–522.

(4) Kutes, Y.; Ye, L.; Zhou, Y.; Pang, S.; Huey, B. D.; Padture, N. P. Direct observation of ferroelectric domains in solution-processed $CH_3NH_3PbI_3$ perovskite thin films. *J. Phys. Chem. Lett.* **2014**, *5*, 3335–3339.

(5) Pazos-Outón, L. M.; Szumilo, M.; Lamboll, R.; Richter, J. M.; Crespo-Quesada, M.; Abdi-Jalebi, M.; Beeson, H. J.; Vrućinić, M.; Alsari, M.; Snaith, H. J. et al. Photon recycling in lead iodide perovskite solar cells. *Science* **2016**, *351*, 1430–1433.

(6) Zhu, X.-Y.; Podzorov, V. Charge carriers in hybrid organic-inorganic lead halide perovskites might be protected as large polarons. *J. Phys. Chem. Lett.* **2015**, *6*, 4758–4761.

(7) Azarhoosh, P.; McKechnie, S.; Frost, J. M.; Walsh, A.; Van Schilfgaarde, M. Research update: Relativistic origin of slow electron-hole recombination in hybrid halide perovskite solar cells. *APL Mater.* **2016**, *4*, 1–8.

(8) Zheng, F.; Tan, L. Z.; Liu, S.; Rappe, A. M. Rashba spin-orbit coupling enhanced carrier lifetime in $CH_3NH_3PbI_3$. *Nano Lett.* **2015**, *15*, 7794–7800.

(9) Hutter, E. M.; Gélvez-Rueda, M. C.; Osherov, A.; Bulović, V.; Grozema, F. C.; Stranks, S. D.; Savenije, T. J. Direct-indirect character of the bandgap in methylammonium lead iodide perovskite. *Nat. Mater.* **2016**, *16*, 115–120.

(10) Li, J.; Haney, P. M. Optical spintronics in organic-inorganic perovskite photovoltaics. *Phys. Rev. B* **2016**, *93*, 155432.

(11) Li, J.; Haney, P. M. Circular photogalvanic effect in organometal halide perovskite $CH_3NH_3PbI_3$. *Appl. Phys. Lett.* **2016**, *109*, 193903.

(12) Moser, J.-E. Perovskite photovoltaics: Slow recombination unveiled. *Nat. Mater.* **2016**, *16*, 4–6.

(13) Etienne, T.; Mosconi, E.; De Angelis, F. Dynamical origin of the Rashba effect in organohalide lead perovskites: A key to suppressed carrier recombination in perovskite solar cells? *J. Phys. Chem. Lett.* **2016**, *7*, 1638–1645.

(14) Yu, Z. G. The Rashba effect and indirect electron-hole recombination in hybrid organic-inorganic perovskites. *Phys. Chem. Chem. Phys.* **2017**, *19*, 14907.

(15) Kirchartz, T.; Rau, U. Decreasing radiative recombination coefficients via an indirect band gap in lead halide perovskites. *J. Phys. Chem. Lett.* **2017**, *8*, 1265–1271.

(16) Bychkov, Y. A.; Rashba, É. I. Properties of a 2D electron-gap with lifted spectral degeneracy. *JETP Lett.* **1984**, *39*, 78–81.

(17) Kim, M.; Im, J.; Freeman, A. J.; Ihm, J.; Jin, H. Switchable S = 1/2 and J = 1/2 Rashba bands in ferroelectric halide perovskites. *Proc. Natl. Acad. Sci. U.S.A.* **2014**, *111*, 6900–6904.

(18) Stroppa, A.; Di Sante, D.; Barone, P.; Bokdam, M.; Kresse, G.; Franchini, C.; Whangbo, M.-H.; Picozzi, S. Tunable ferroelectric polarization and its interplay with spin-orbit coupling in tin iodide perovskites. *Nat. Commun.* **2014**, *5*, 5900.

(19) Kepenekian, M.; Robles, R.; Katan, C.; Sapori, D.; Pedesseau, L.; Even, J. Rashba and Dresselhaus effects in hybrid organic-inorganic perovskites: From basics to devices. *ACS Nano* **2015**, *9*, 11557–11567.

(20) Kepenekian, M.; Even, J. Rashba and Dresselhaus couplings in halide perovskites: Accomplishments and opportunities for spintronics and spin-orbitronics. *J. Phys. Chem. Lett.* **2017**, *8*, 3362–3370.

(21) Hu, S.; Gao, H.; Qi, Y.; Tao, Y.; Li, Y.; Reimers, J. R.; Bokdam, M.; Franchini, C.; Di Sante, D.; Stroppa, A. et al. Dipole order in halide perovskites: Polarization and Rashba band splittings. *J. Phys. Chem. C* **2017**, 23045–23054.

(22) Kioupakis, E.; Yan, Q.; Steiauf, D.; Van de Walle, C. G. Temperature and carrier-density dependence of Auger and radiative recombination in nitride optoelectronic devices. *New J. Phys.* **2013**, *15*, 125006.

(23) Tress, W. Perovskite solar cells on the way to their radiative efficiency limit - Insights into a success story of high open-circuit voltage and low recombination. *Adv. Energy Mater.* **2017**, *7*, 1602358.

(24) Dresselhaus, G. Spin-orbit coupling effects in zinc blende structures. *Phys. Rev.* **1955**, *100*, 580–586.

(25) Manchon, A.; Koo, H. C.; Nitta, J.; Frolov, S. M.; Duine, R. A. New perspectives for Rashba spin-orbit coupling. *Nat. Mater.* **2015**, *14*, 871–882.

(26) Stroppa, A.; Quarti, C.; De Angelis, F.; Picozzi, S. Ferroelectric polarization of $CH_3NH_3PbI_3$: A detailed study based on density functional theory and symmetry mode analysis. *J. Phys. Chem. Lett.* **2015**, *6*, 2223–2231.

(27) Motta, C.; El-Mellouhi, F.; Kais, S.; Tabet, N.; Alharbi, F.; Sanvito, S. Revealing the role of organic cations in hybrid halide perovskite $CH_3NH_3PbI_3$. *Nat. Commun.* **2015**, *6*, 7026.

(28) Kresse, G.; Furthmüller, J. Efficient iterative schemes for ab initio total-energy calculations using a plane-wave basis set. *Phys. Rev. B* **1996**, *54*, 11169–11186.

(29) Heyd, J.; Scuseria, G. E.; Ernzerhof, M. Hybrid functionals based on a screened Coulomb potential. *J. Chem. Phys.* **2003**, *118*, 8207–8215.

(30) Ogomi, Y.; Morita, A.; Tsukamoto, S.; Saitho, T.; Fujikawa, N.; Shen, Q.; Toyoda, T.; Yoshino, K.; Pandey, S. S.; Ma, T. et al. $CH_3NH_3Sn_xPb_{1-x}I_3$ perovskite solar cells covering up to 1060 nm. *J. Phys. Chem. Lett.* **2014**, *5*, 1004–1011.

(31) Blöchl, P. E. Projector augmented-wave method. *Phys. Rev. B* **1994**, *50*, 17953–17979.

(32) Monkhorst, H. J.; Pack, J. D. Special points for Brillouin-zone integrations. *Phys. Rev. B* **1976**, *13*, 5188–5192.

(33) Weller, M. T.; Weber, O. J.; Henry, P. F.; Di Pumpo, A. M.; Hansen, T. C. Complete structure and cation orientation in the perovskite photovoltaic methylammonium lead iodide between 100 and 352 K. *Chem. Commun.* **2015**, *51*, 4180–4183.

(34) Zhang, X.; Liu, Q.; Luo, J.-W.; Freeman, A. J.; Zunger, A. Hidden spin polarization in inversion-symmetric bulk crystals. *Nat. Phys.* **2014**, *10*, 387–393.

(35) Gajdoš, M.; Hummer, K.; Kresse, G.; Furthmüller, J.; Bechstedt, F. Linear optical properties in the projector-augmented wave methodology. *Phys. Rev. B* **2006**, *73*, 045112.